RSC Advances

ROYAL SOCIETY OF CHEMISTRY

www.rsc.org/advances

RSC Advances

PAPER

Controlling synthesis and application of nanocrystalline spherical and ordered mesoporous alumina with high thermal stability

Received 00th January 20xx,
Accepted 00th January 20xx

DOI: 10.1039/x0xx00000x

www.rsc.org/

Fang Liu,[a] Xiaohai Zheng,[a] Jiebo Chen,[b] Ying Zheng,[a]* Lilong Jiang[c]

High thermal stability nanocrystalline spherical mesoporous alumina (NSMA) and ordered mesoporous alumina (OMA) were synthesized in an acetic acid assisted sol-gel system by adjusting the mole ratio of n(acetic acid)/n(Al) and synthesis temperature to control the competition between the colloidal surface free energy (*F*) and the free energy of mesostructure self-assemble (ΔG). When *F* was dominant, with the mole ratio of n(acetic acid)/n(Al) set as 0.05-0.15 and formation and aging temperature of precursor solution at 30 °C, the obtained alumina displayed spherical morphology, and the nanocrystalline spherical mesoporous alumina dispersed well even the calcination temperature up to 1100 °C; while the ordered mesoporous alumina was obtained with the increasing influence of ΔG when the mole ratio of n(acetic acid)/n(Al) set as 0.10 and lower formation and aging temperature at 20 °C, and it retained a certain ordered structure with the specific surface area of 125 m^2 g^{-1} even the calcination temperature up to 1000 °C, indicating the excellent thermal stability of its pore structure. Taking the as-synthesized aluminas as carriers, Pd-supported catalysts were obtained and its catalytic activity for CO and C_3H_6 oxidation were significantly improved compared to commercial alumina.

1. Introduction

Mesoporous materials have been applied in many areas because of their special properties including highly uniform channels, large surface area and narrow pore size distribution [1, 2], among which mesoporous alumina was widely used as catalyst carriers [3], adsorbents [4] and heat insulating materials [5] due to its high thermal stability, favorable textural properties and intrinsic acid–base characteristics. The properties of alumina are determined predominantly by the crystal phase, pore structure and morphology [6] so that the synthesis of nanocrystalline alumina with controlled morphology [7] and OMA have attracted great attention in recent years. Nanocrystalline alumina with controlled morphologies such as blets [8], tubes, sheets [9], wires [10], whiskers [11] and rods [12] have been synthesized. When it comes to catalyst carrier, morphology and pore structure of materials have a great influence on the heat transfer and mass transfer. Nanocatalysts are characterised by the unique nanoscale properties that originate from their highly reduced dimensions, and extensive studies over the past few decades have demonstrated that the size and shape of a catalyst particle on the nanometre scale profoundly affect its reaction performance [12]. In particular, controlling the catalyst particle morphology allows a selective exposure of a larger fraction of the reactive facets on which the active sites can be enriched and tuned. J.Gascon *et al.* [13] discussed the diffusion of reactants and products between the carrier and the catalytic active sites at mesolevel, indicating that the orderly morphology would be more conducive to mass and heat transfer and it might improve the activity of supported-catalyst.

Meanwhile, the synthesis and application of OMA have aroused people's attention because of the crystal phase and the pore structure of alumina having great influence on its performance. Niesz *et al.* [14] first reported the synthesis of 2D hexagonal mesoporous alumina by a sol-gel route, which simplify the synthetic process of OMA, however, the procedure required strictly controlled aging condition under N_2 flow. Yuan *et al.* [15] using a modified sol-gel process synthesized the OMA in air by employing citric acid as interfacial protector and the highly ordered mesoporous structure was resistant to high temperature up to 1000 °C, which provides a new method for the synthesis of OMA. Our group extended this approach to prepare a series of OMA with high specific surface area, large pore size and high thermal stability by introducing carboxylic acids with special structure such as a mixture of salicylic acid and citric acid [16], *o*-phthalic acid [17] and *p*-aminobenzoic acid [18] as interfacial protectors or silicon [19], cerium and zirconium [20] as dopants to further stabilize the structure of OMAs. Moreover, the application of the alumina-based catalysts with specific morphology or ordered pore structure has gained much attention: catalytic materials of alumina and lanthana doped alumina supported nanosize palladium particles have been successfully prepared and the catalytic activity test of Pd-coated γ-Al_2O_3-spheres for CO and NO_x oxidation indicated that it had a clearly better light-off behavior as fresh compared to the reference sample [21]; Using OMA with 8 mol% Ce as carrier, the precious metals supported meso-8CeAl catalyst was synthesized for CO

[a] College of Chemistry and Materials Science, Fujian Normal University, Fuzhou, Fujian 350007, China. E-mail: zhn63200@163.com; Fax: +86 591 83464353; Tel: +86 591 83464353
[b] College of Chemistry and Chemical Engineering, Fujian Normal University, Fuzhou, Fujian 350007, China
[c] National Engineering Research Center of Chemical Fertilizer Catalyst, Fuzhou University, Fuzhou, Fujian 350002, China.

conversion and it exhibited excellent catalytic activity at room temperature with 100% conversion occurring at 26 °C [22]. The results demonstrated that alumina-based catalysts with specific morphology or ordered pore structure possessed excellent catalytic property compared to commercial alumina.

Many methods, such as hydrothermal [23], precipitation [24], cation-anion double hydrolysis [25] and self-assembly method [26-28], have been used to synthesize mesoporous oxide materials. Among these routes, sol-gel process combined with evaporation-induced self-assembly (EISA) process was a best option to synthesize mesoporous oxide materials for its simple synthetic process and controllable synthesis conditions. Besides, structure-directing agents of sol-gel process was optional including biological template [2] and chemical template [15, 29]. Mesoporous aluminas prepared by employing self-assembly method in a sol-gel system also attract a lot of attention. It is considered that in the process of the formation of alumina, the morphology of as-prepared alumina is powerfully influenced by the competition of the colloidal surface free energy (*F*) and the free energy self-assemble (ΔG) [30]. When *F* is dominant, the morphology with large curvature will be generated in order to minimize the surface energy; with the increasing influence of ΔG, particles will develop together with the formation of mesostructure, therefore, mesoporous materials with crystal-like morphologies could be generated. We suppose that using acetic acid as interfacial protector is conductive to the high specific surface area and thermal stability of OMA for its volatility makes it easier to be removed at lower temperature and leave the pore structure less changed, meanwhile influenced the competition of *F* and ΔG. Herein, in this paper, in an acetic acid assisted sol-gel system, by adjusting synthesis conditions such as the mole ratio of n(acetic acid)/n(Al) and synthesis temperature to control the colloidal surface free energy (*F*) and the competition between ΔG, we successfully obtained NSMA and OMA both in possession of high thermal stability, which provide a valuable method to the controlling synthesis of alumina with specific morphology or ordered pore structure. In addition, taking NSMA and OMA as carriers, we prepared the Pd-supported catalysts to study the catalytic activity for CO and C_3H_6, the results indicating that compared to commercial alumina (CA), the complete conversion temperature of CO (C_3H_6) to CO_2 and H_2O was greatly reduced.

2. Experimental

2.1 Synthesis of NSMA and OMA

In a typical synthesis of NSMA, 1 g Pluronic P123 (EO20PO70EO20, Mav=5800) was added into 20 mL anhydrous ethanol at 30 °C, then a certain amount of hydrochloric acid (37 wt%) was added to dissolve the P123. After that, different amount of acetic acid and 0.01 mol of $Al(OiP)_3$ were introduced with vigorous stirring and adjusted the pH value of *ca.* 0.6 by hydrochloric acid in the synthetic system. The mixture was stirried for 5 h and aged at same temperature for 24 h in air. The gels were transferred into a 60 °C drying oven to undergo the solvent evaporation process, then the white xerogels were obtained. Calcination was carried out at 400 °C for 4 h with a heating rate of 1 °C min^{-1}. High-temperature treatment was carried out in air for 1 h with a heating rate of 10 °C min^{-1} to 800 °C, 1000 °C, 1100 °C, respectively after calcination at 400 °C.

The OMA was obtained with same synthesis conditions as NSMA by only changing the synthesis temperature and controlling it at 20 °C.

The prepared samples were labeled as xAA-30 when synthesis temperature was 30 °C and xAA-20 when synthesis temperature was 20 °C (x stands for the mole ratio of n(acetic acid)/n(Al), x = 0, 0.05, 0.10, 0.15, 0.20; AA stands for alumina with the addition of acetic acid).

2.2 Catalysts Preparation

Supported Pd catalysts containing 0.5 wt% Pd (theoretic value) were prepared by incipient wetness impregnation method using an aqueous $Pd(NO_3)_2$ solution as the Pd precursor. Briefly, $Pd(NO_3)_2$ was dissolved in de-ionized water, and then a certain amount of as-synthesized aluminas which calcined at 400 °C were impregnated in this solution (denoted hereinafter as Pd/xAA-30(20)), and for comparison, commercial alumina (Alfa Aesar) supported Pd catalysts was also prepared (denoted hereinafter as Pd/CA). Impregnated samples were dried in ambient air at 110 °C for 5 h and then calcined at 800 °C and 1000 °C for 1 h with a heating rate of 10 °C min^{-1}, respectively.

2.3 Characterization

The morphologies of the samples were imaged by Scanning electron microscopy (SEM) on a Hitachi S-4800 electron microscope; The Brunauer-Emmett-Teller (BET) surface area and Barrett-Joyner-Halenda (BJH) pore size distribution were derived by Quantachrome Nova 4200 volumetric analyzers; X-ray diffraction (XRD) patterns were recorded on a Philips X'pert pro MPD diffractometer; Transmission electron microscopy (TEM) images were taken using FEI Tecnai G2 F20 S-TWIN (200 kV) electron microscope.

On-line analysis of catalyst activity was carried out in a continuous flow microreactor by GC-14 gas chromatographic analyzer equipped with TCD detector gas chromatographic analyzer and FULI 9750 gas chromatographic analyzer equipped with a hydrogen flame detector to analysis the composition of source gas and products.

Typically, 100 mg of catalyst was placed in the quartz tube of the inner diameter of 8 mm as a fixed bed reactor, then pass into the mixture (the gas initially present with a flow of 1670 mL g^{-1} h^{-1}, CO of 0.41%, C_3H_6 of 810 ppm, O_2 of 0.56%, helium as balance gas). Conversion rate of CO and C_3H_6 under different temperature was recorded and the complete conversion temperature $T_{100\%}$ was taken as the index of the evaluation of activity. Calculating formula for conversion rate was:

$$X = \frac{\varphi_{in} - \varphi_{out}}{\varphi_{in}} \times 100\%$$

X: conversion rata of CO (C_3H_6).

φ_{in}: the volume of CO (C_3H_6) of source gas.

φ_{out}: the volume of CO (C_3H_6) of products.

CO temperature-programmed desorption (CO-TPD) and H_2 temperature-programmed reduction (TPR) characterizations was tested in U.S. Mcirometritics Autochem 2920 automatic adsorption instrument. In a typical procedure of CO-TPD, the catalyst (*ca.* 300 mg) was reduced in a H_2 stream at 350 °C for 1 h and subsequently flushed with a He stream for 1.5 h to remove impurities and H_2

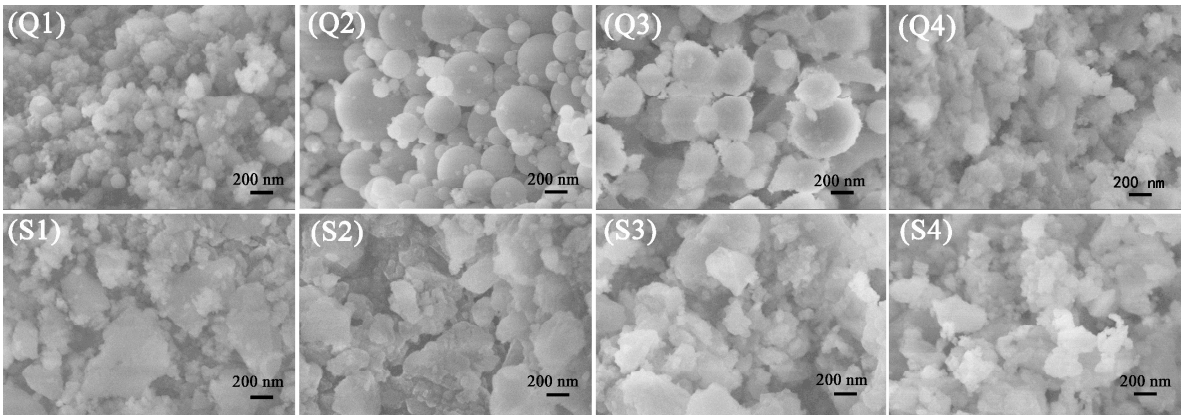

Figure 1. SEM images of the samples synthesized at different temperatures (Q1: 0.05AA-30, Q2: 0.10AA-30, Q3: 0.15AA-30, Q4: 0.20AA-30; S1: 0.05AA-20, S2: 0.10AA-20, S3: 0.15AA-20, S4: 0.20AA-20) calcined at 400 °C

adsorbed on the surface of the catalyst, then cooled to room temperature to adsorbed CO. The chemisorption of CO was measured by the pulse method, the dispersions, specific metal surface areas and sizes of Pd particles were calculated from the cumulative volume of CO adsorbed during pulse chemisorption. As for H_2-TPR characterization, 300 mg of the sample was packed into a reactor, and oxidized by oxygen for 1 h at 450 °C, then purged by He for 1 h at 300 °C to remove impurities, and cooled down to room temperature. TPR traces of the samples were pursued in a reductive flow of 30 mL min^{-1} 10% H_2-Ar, heated from room temperature to 800 °C at a rate of 10 °C min^{-1}.

In situ-diffuse reflectance infrared Fourier transform spectroscopy (*in situ*-DRIFTS) was carried out on a Nicolet-6700 spectrometer at a spectral resolution of 2 cm^{-1} (accumulating 64 scans). About 40 mg of the fine powder catalyst was placed firmly in the diffuse reflectance cell. The catalyst was pretreated under a He flow at a rate of 10 °C/min from room temperature to 300 °C. The catalyst was reduced under a 10%H_2/Ar flow for 1h and vacuumized. Then cooled down to room temperature under a He flow. The spectra of CO absorbed were recorded after the sample was exposed to 1%CO/He. Finally, purged the catalyst by He for 30 min and recorded the spectra again.

X-ray photoelectron spectroscopy (XPS) was performed on a Thermo ESCALAB 250 spectrometer with Al Kα radiation (1486.6 eV). All of the XPS data were calibrated using the binding energy of C 1s (284.6 eV) as a standard.

3.Results and discussion

3.1 Morphology, structure and properties of NSMA and OMA

Figure 1 shows the SEM images of the calcined samples synthesized at different temperatures. It can be observed spherical nanoparticles when the mole ratio of n(acetic acid)/n(Al) ranging from 0.05 to 0.15 and synthesized at 30 °C (Figure 1Q1, Q2, Q3), and the nanosize spheres of 0.10AA-30 present a most uniform size in a certain range of 100-300 nm. However, it failed to synthesize the alumina with regular morphology when the synthesis temperature was 20 °C (Figure 1S1, S2, S3, S4). The phenomenon might be ascribed to the competition between the colloidal surface free energy (*F*) and the free energy of mesostructure self-assemble (ΔG) [30]. A certain mole ratio of n(acetic acid)/n(Al)=0.05-0.15 strengthened the interaction between aluminum precursor and template, meanwhile influenced the competition of *F* and ΔG. The self-assembly of Al^{3+} forming the 3D cross-linked inorganic/organic framework which made it easy to reunite into various morphologies. When synthesized at 30 °C, *F* became dominant with higher internal energy in the synthetic system and the precursor solution evaporated rapidly in the aging process. To decrease the internal energy and counterbalance the sudden concentration change of the micelle in the process of rapid solvent evaporation, the liquid crystal phase developed together to generate the morphology with large curvature in order to minimize the surface area and therefore *F*, so the morphology of product would be spherical, and the specific surface area would be reduced accompanying less ordered pore structure. However, when the synthesis temperature was 20 °C, ΔG became dominant and products would preserve the intrinsic liquid crystal structure with ordered pore structure and form irregular morphology, it will be further discussed in detail.

Table 1. Specific surface area of the calcined samples (S_{BET}/m^2 g^{-1})

Samples	Synthesized at 30 °C		Synthesized at 20 °C	
	800 °C	1000 °C	800 °C	1000 °C
0AA	118	66	210	96
0.05AA	137	76	279	111
0.10AA	149	82	303	125
0.15AA	144	72	305	120
0.20AA	125	68	223	104

The BET surface areas of the calcined samples are summarized in Table 1. Compared with the sample prepared without addition of acetic acid, the surface areas of the samples first increases and then decreases with the increasing mole ratio of n(acetic acid)/n(Al) in the range of 0.05-0.20. As shown in Table 1, the specific surface

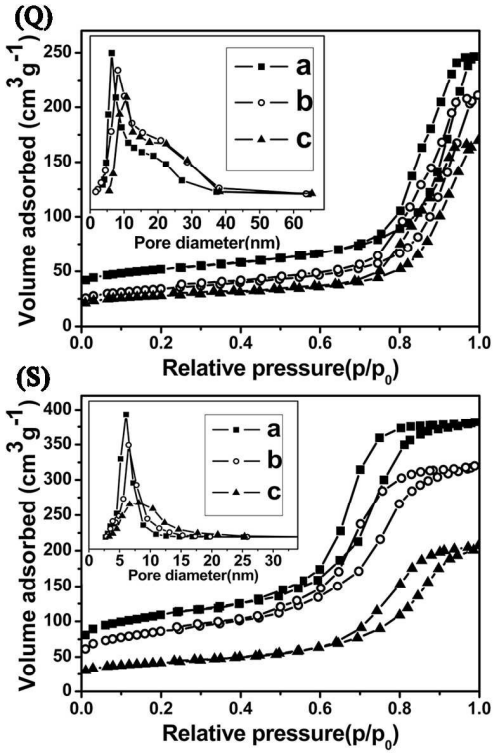

Figure 2. Nitrogen adsorption-desorption isotherms and pore size distribution curves of 0.10AA-30 (Q) and 0.10AA-20 (S) (a: 400 °C, b: 800 °C, c: 1000 °C)

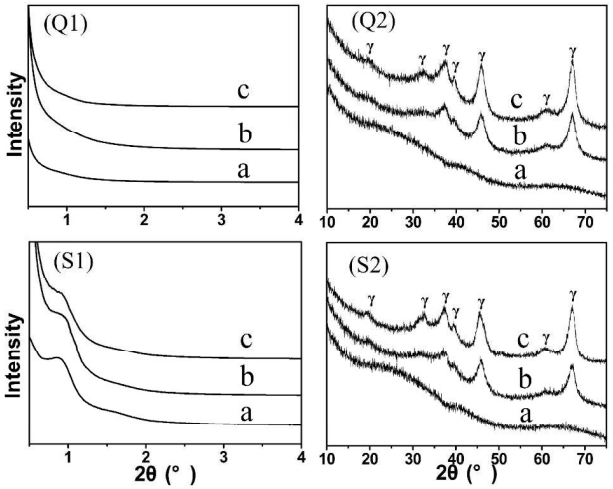

Figure 3. Small-angle XRD patterns and Wide-angle XRD patterns of 0.10AA-30 (Q1, Q2) and 0.10AA-20 (S1, S2) calcined at different temperatures (a: 400 °C, b: 800 °C, c: 1000 °C)

area of xAA-20 series are higher than xAA-30 series, and 0.10AA-30 and 0.10AA-20 exhibit the best textual property among the xAA-30 series and xAA-20 series with specific surface area of 82 m^2 g^{-1} and125 m^2 g^{-1}, respectively, even after calcination at 1000 °C. The two samples will be taken for further characterization.

The nitrogen adsorption-desorption isotherms and corresponding pore size distribution are shown in Figure 2. The sample 0.10AA-30 treated at different temperatures all yield type-IV curves (Figure 2Q), which demonstrates the existence of mesoporous structure [31]. The hysteresis loop close at a higher relative pressure p/p_0 of 0.7, indicating the larger pore size of the samples [32], and the double distribution of the pores shown in Figure 2Q belong to channel structure of mesoporous alumina (6-10 nm) and bulk pore stacking by the uniform nano-alumina particles (15-23 nm). The isotherms of 0.10AA-20 display type-IV curves with H1-type hysteresis loops after calcination at different temperatures with a mean value pore size (*ca*. 8 nm) (Figure 2S), which accord with the TEM images of Figure 4S, suggesting the existence of the uniform cylindrical mesoporous [33]. Meanwhile, the 0.10AA-20 still exhibit large surface area of 125 m^2 g^{-1} after calcination at 1000 °C, indicating its excellent thermal stability.

As shown in Figure 3Q1, no distinguishable diffraction peak of 0.10AA-30 treated at different temperatures is observed. However, the sample 0.10AA-20 appear apparent diffraction peaks around 1° (Figure 3S1), which, according to the TEM observation, can be attributed to 2D hexagonal *p6mm* symmetry [15, 34], and the intensity of diffraction peaks gradually reduce with the increasing of calcination temperature, suggesting the partly loss of ordered mesostructure. It is thus clear that the free energy of self-assemble(ΔG) was responsible for the as-prepared alumina mesostructure, with the mole ratio of n(acetic acid)/n(Al)=0.10 and low synthesis synthesis temperature at 20 °C. In general, in the presence of Cl^-, the complexation of Cl^- with Al^{3+} might disturb the charge balance between organic template and Al^{3+}, and then interfered Al^{3+} self- assembly process on the interface, resulting in the disordered mesostructure [35]. With the introduction of acetic acid, on the one hand, the carboxyl of the acetic acid could preferentially coordinate with Al^{3+} by replacing the -OR (R: alkyl) which connected directly with Al^{3+} originally, restraining the interference of Cl^- to the self-assembly of Al^{3+} and thus controlling the hydrolysis-condensation rate of the aluminum source [36], which conducive to the formation of orderly channel. On the other hand, the interaction between the carboxyl and polyethylene group of the block copolymer by the hydrogen bonding and Van der Waals forces anchored the Al^{3+} upon the interface of block copolymer. With synthesis temperature at 20 °C, the internal energy of system was lower and the slow solvent evaporation in the aging process resulted in Al^{3+} self-assembly more sufficient, which enhanced the influence of ΔG, so micelle developed together with the formation of ordered mesostructure, moreover, the volatility of the acetic acid made it easier to be removed at lower temperature and would leave the assembled pore structure less changed, so the texture of final mesoporous materials would preserve the intrinsic liquid crystal structure with ordered pore structure, and the morphology aggregated irregularly.

The wide-angle XRD patterns given in Figure 3Q2 S2 show the similar phase transition property of 0.10AA-30 and 0.10AA-20. With the increasing of calcination temperature, marked diffraction peaks

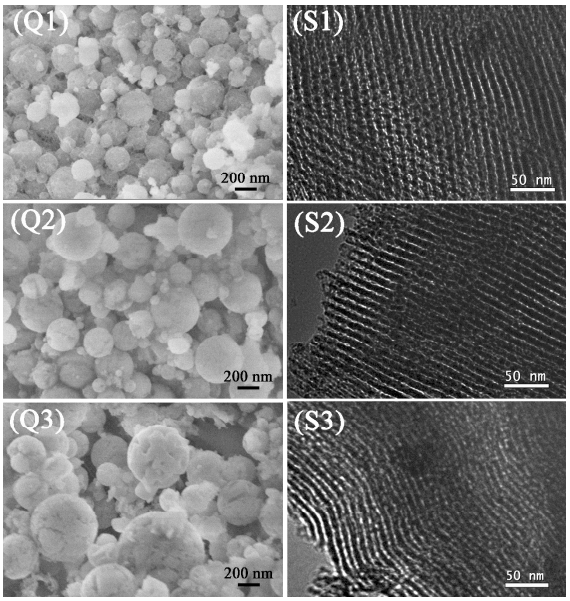

Figure 4. SEM images of 0.10AA-30 (Q1: 800 °C, Q2: 1000 °C, Q3: 1100 °C) and the TEM images of 0.10AA-20 (S1: 400 °C, S2: 800 °C, S3: 1000 °C)

of the samples calcined at 800 °C are observed at 39.5°, 45.9°, 60.9°, 67.0°, corresponding to the γ-Al_2O_3 phase [20], and no other crystalline phase can be observed even after treatment at 1000 °C. It demonstrated that γ-Al_2O_3 phase didn't transform to other phase although there was a tendency for Al^{3+} to adopt a higher coordination number at a high temperature [37, 38], and pure γ-phase alumina with high thermal stability was obtained.

As shown in Figure 4, the SEM images of the nanosize alumina spheres (0.10AA-30) appear perfect surface (Figure 4Q1) after calculation at 800 °C. With the increasing of the calcination temperature, the surface of spheres began to appear flaw (Figure 4Q2, Q3). But even the calcination temperature up to 1100 °C the spheres still not aggregated and retained the spherical morphology (Figure 4Q3), which is promising for practical application of the catalyst carrier at high temperature operation. The TEM images of 0.10AA-20 calcined at different temperatures were shown as Figure 4S1 S2 S3. It can be observed that ordered mesoporous structure with 2D hexagonal symmetry [19] is still retained after treated at 1000 °C, which matches well with the XRD results. These results forcefully prove that the prepared ordered mesoporous γ-Al_2O_3 characterized with high thermal stability.

3.2 Catalytic activity, morphology, structure and properties of catalysts

The catalytic activity of Pd-supported catalysts for CO and C_3H_6 oxidation using CA, 0.10AA-30 and 0.10AA-20 as carriers are shown in Figure 5. The results indicate that the catalytic activity for catalysts after calcination at 800 °C, corresponding to Pd/CA, Pd/0.10AA-30 and Pd/0.10AA-20, the completely oxidized temperature ($T_{100\%}$) of CO and C_3H_6 were 280 °C, 250 °C, 220 °C and 300 °C, 280 °C, 250 °C, respectively. And for catalysts after calcination at 1000 °C, corresponding to Pd-CA, Pd-0.10AA-30 and

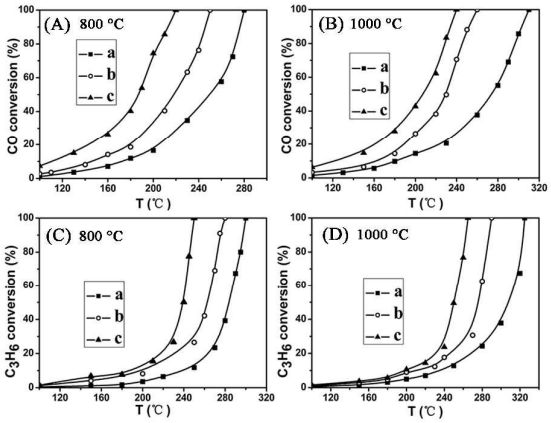

Figure 5. Catalytic activity of catalysts (a: Pd/CA, b: Pd/0.10AA-30 and c: Pd/0.10AA-20)

Table 2. Metallic dispersion, metallic surface area and active particle diameter of fresh catalysts

Catalyst	Metal dispersion (%)[(a)]	Metallic surface area (m^2g^{-1})	Active particle diameter (nm)
Pd-CA (800 °C)	17.51	43.78	6.45
Pd/0.10AA-30 (800 °C)	23.78	67.69	5.22
Pd/0.10AA-20 (800 °C)	30.24	72.88	3.82
Pd/CA (1000 °C)	6.42	15.07	17.97
Pd/0.10AA-30 (1000 °C)	9.46	22.67	11.58
Pd/0.10AA-20 (1000 °C)	14.33	33.25	8.53

(a) CO chemisorption using average CO:Pd stoichiometry of 1:1.

Pd-0.10AA-20, the terminal CO and C_3H_6 species completely disappeared at 310 °C, 260 °C, 240 °C and 325 °C, 290 °C, 265 °C, respectively. It also can be seen from the figure that C_3H_6 conversion increases abruptly when the reaction temperature reached at light-off temperature ($T_{50\%}$). It was consider that the hexagonal alumina exhibits faster kinetics than those obtained with the wormhole-like alumina counterparts [39], and the dispersion of metal particles was proportional to the specific surface area which had a striking influence on the activity of CO and C_3H_6 oxidation. The conclusion will be further validated next.

CO-TPD was taken to measure Pd dispersion of different fresh catalysts. After reduction preprocessing in a H_2 stream, the PdO particles on the catalysts have been reduced to Pd particles. It can be summarized from Table 2 that dispersion of Pd is in the order Pd/CA < Pd/0.10AA-30 < Pd/0.10AA-20, and metallic surface area gradually increase, active particle diameter gradually decrease. And compared to the fresh catalyst calcined at 800 °C, the dispersion of Pd and metallic surface of the catalyst calcined at 1000 °C decreased, and active particle diameter increased. The results were in accordance with catalytic activity of the samples and further confirmed that the metal dispersion of catalyst was one of the influence factors on catalytic activity. So that we could speculate

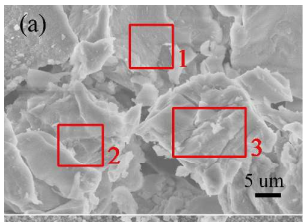

Element	Weight %		
	1	2	3
O(K)	51.24	50.36	53.44
Al(K)	48.35	49.20	46.09
Pd(L)	0.41	0.44	0.47

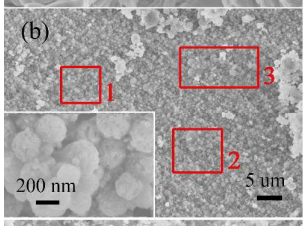

Element	Weight %		
	1	2	3
O(K)	52.42	48.54	50.16
Al(K)	47.12	50.98	49.39
Pd(L)	0.46	0.48	0.45

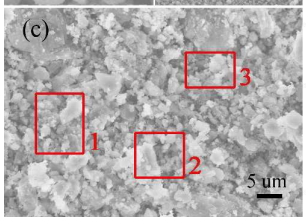

Element	Weight %		
	1	2	3
O(K)	51.50	50.32	50.39
Al(K)	48.05	49.20	49.17
Pd(L)	0.45	0.48	0.44

Figure 6. SEM-EDX of fresh catalysts calcined at 1000 °C (a: Pd/CA, b: Pd/0.10AA-30 and c: Pd/0.10AA-20)

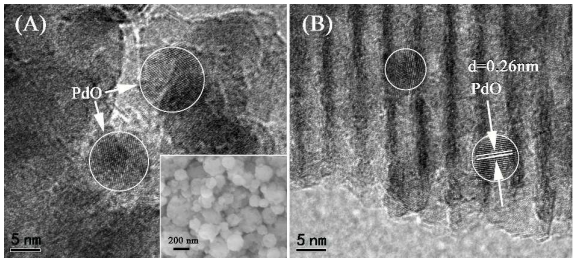

Figure 7. HRTEM and SEM (inset of A) images of used catalysts calcined at 1000 °C (A: Pd/0.10AA-30 B: Pd/0.10AA-20)

that if a carrier with not merely a regular morphology but also ordered channel structure should have higher catalytic activity.

The SEM and the corresponding EDX spectra of fresh catalysts calcined at 1000 °C are shown in Figure 6. The SEM images indicate that Pd/CA displays large clumps with undefined shape and Pd/0.10AA-30 shows spherical particles and the morphologies which similar to its carriers. The morphology and particle size of Pd/0.10AA-20 are also similar to its carrier. The results indicate that the original morphology of as-synthesized aluminas (Figure 1Q2, S2) were no changed after supported Pd by incipient wetness impregnation. The corresponding EDX spectra of various catalysts confirms the presence of O, Al and Pd, and the elemental analysis determined from the EDX indicates that the content of Pd is 0.44%, 0.46% and 0.46% (average value) corresponding to Pd-CA, Pd-0.10AA-30 and Pd-0.10AA-20, respectively, which is close to the theoretic value in the initial composition (0.5%).

In order to explore the detailed characterization on the active phase and the thermal stability of the catalysts, the used catalysts were

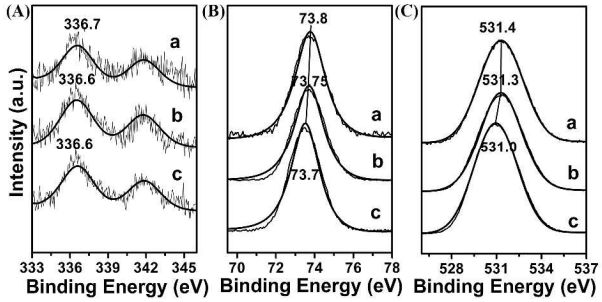

Figure 8. XPS spectra of Pd 3d (A), Al 2p (B) and O 1s (C) of fresh catalysts (a: Pd/CA, b: Pd/0.10AA-30 and c: Pd/0.10AA-20)

examined by HRTEM and SEM. Figure 7 presents HRTEM micrographs of the used catalysts calcined at 1000 °C. The small PdO nano particles exhibit a good dispersed state on the support surface (as labeled by the circles) and are isolated from each other, so it is deduced that the active sites of PdO can be fully exposed to reactant gases so as to improve the activity of catalysts [40], and the particle sizes of PdO for Pd/0.10AA-20 and Pd/0.10AA-20 are 5-7 and 8-10 nm, respectively. The CO-TPD rusults shown in table 2 show the larger paticle size than the HRTEM, which may due to the statistical method using the absorption model of CO to Pd was 1:1 in the CO-TPD, but there also exist bridge-bound with the CO to Pd of 1:2. Therefore, the PdO nano particles can embed in the Pd/0.10AA-20 mesopore as shown in Figure 7B. The inset of Figure 7A shows the fine spherical morphology of Pd/0.10AA-30 and Figure 7B exhibits ordered pore structure of Pd/0.10AA-20, indicating the high thermal stability of synthetic catalysts.

XPS was taken to illustrate the metallic states of active component [41]. Figure 8 shows XPS spectra of Pd 3d (A), Al 2p (B) and O 1s (C) XPS spectra of fresh catalysts. From the results given in Figure 8A it can be seen that the binding energy (BE) of 336.6, 336.6 and 336.7 eV for the Pd 3d5 level in Pd/CA, Pd/0.10AA-30 and Pd/0.10AA-20, respectively, are typical of the +2 oxidation state [42], which lower than actual BE value for the Pd 3d5 of pure PdO peak of 337.0 eV.

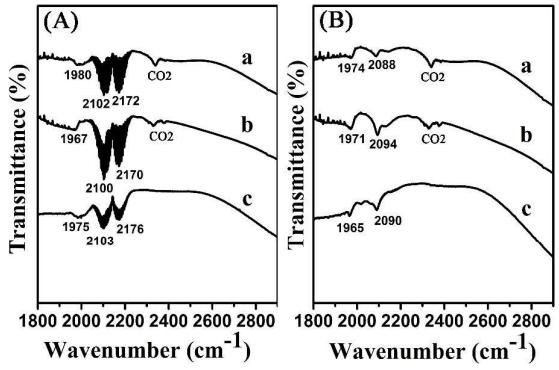

Figure 9. *In situ*-DRIFTS spectras of fresh catalysts calcined at 1000 °C absorbed CO for 1h (A) and purge by helium (B) (a: Pd/CA, b: Pd/0.10AA-30 and c: Pd/0.10AA-20)

And the BE of Al 2p for Pd/CA, Pd/0.10AA-30 and Pd/0.10AA-20 are 73.8, 73.75 and 73.7 eV, which lower than pure γ-Al_2O_3 (74.3 eV). The results above reveal the existence of interaction in the interface of palladium particles and the support after the calcination process. The BE of O 1s for Pd/CA, Pd/0.10AA-30 and Pd/0.10AA-20 are 531.5, 531.8 and 531.9 eV, which is close to the BE of O 1s for pure Al_2O_3 (531.5 eV) (the BE of pure PdO was 530.7 eV), indicating that it was difficult to detect the existence of PdO on the catalysts for the low content of PdO.

In situ-DRIFTS was used to observe CO adsorption on the fresh catalysts, the results for which are shown in Figure 9. For CO adsorption on the catalysts, as can be seen in Figure 9A, the main bands in the C-O stretching frequency range correspond to linearly adsorbed CO at 2035 to 2230 cm^{-1}. The Pd/CA, Pd/0.10AA-30 and Pd/0.10AA-20 show a band assigned to bridge-bonded CO at 1980, 1967 and 1975 cm^{-1}, respectively [43]. The intensity of peaks are gradually increase in the order of Pd/CA < Pd/0.10AA-30 < Pd/0.10AA-20, which coincide with the dispersion of active component in the table 2. After purged the catalyst by He for 30 min, the bands belong to bridge-bonded of CO adsorption still retained, but the linearly bonded obviously weakened, which demonstrates that bridge-bonded is stronger than linearly adsorbed.

Figure 10 shows the nitrogen adsorption-desorption isotherms and corresponding pore size distribution of the fresh catalysts calcined at 1000 °C. All samples display type-IV curves, indicating the existence of mesopores. Compared to catalyst carriers, the texture properties of Pd/0.10AA-30 is not changed obviously with specific surface area of 83 $m^2 g^{-1}$ and bimodal pore size distribution. And Pd/0.10AA-20 still maintains a high specific surface area of 119 $m^2 g^{-1}$ and narrow pore-size distributions. However, Pd/CA exhibits low specific surface area of 56 $m^2 g^{-1}$ and broad pore size distribution after high temperature calcination. Such we could draw a conclusion that catalytic activities of Pd-supported catalysts for CO and C_3H_6 oxidation were significantly affected by the morphology and specific surface area. Pd/0.1AA-30 with a regular spherical structure was beneficial to mass transfer of reactants and products, as well as heat transfer in the reaction process, and its mesoporous structure possessed higher porosity and specific surface area compared to commercial alumina, thus its completely transformation temperature of CO and C_3H_6 oxidation was lower than commercial alumina. Pd/0.1AA-20 with high specific surface area, narrow size-distributed region and ordered mesostructure leading high dispersion of active component Pd, so it has the highest activity for CO and C_3H_6 oxidation.

The XRD patterns of fresh, used and reduced catalysts calcined at 1000 °C are presented in Figure 11. For the catalyst Pd/CA, the fresh sample exhibits some peaks of α-Al_2O_3 (JCPDS 11-0661) at 25.5°, 43.4°, 52.4° and 57.6° as well as characteristic diffraction peak of PdO around 34.3° (JCPDS 75-0584), which indicated that high temperature calcination made commercial alumina phase transformation from γ-Al_2O_3 to α-Al_2O_3 and the aggregation of PdO particles. There are no diffraction peaks of α-Al_2O_3 and PdO observed in Pd/0.10AA-30 and Pd/0.10AA-20, the catalysts keeping high thermal stability. For used Pd/CA, two more PdO peaks appeared, which may be attributed to the active metal distributed on the surface of the carrier, after catalytic reaction of CO and C_3H_6, PdO aggregated partly. For reduced Pd/CA, the peaks of PdO disappear, and appear two Pd peaks, which indicated PdO has been reduced to Pd completely. For Pd/0.1AA-30 and Pd/0.1AA-20, no matter used or reduced samples, there are no peak of PdO or Pd appear compare to the fresh catalysts, which further evidence the

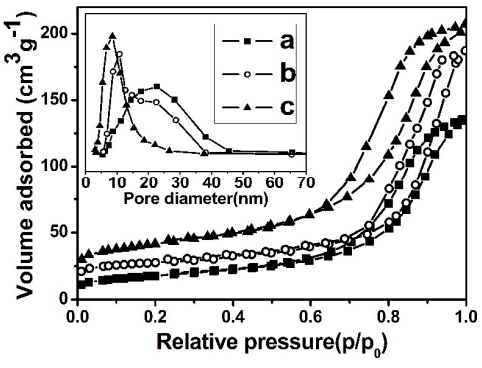

Figure 10. Nitrogen adsorption-desorption isotherms and pore size distribution curves of fresh catalysts calcined at 1000 °C (a: Pd/CA, b: Pd/0.10AA-30 and c: Pd/0.10AA-20)

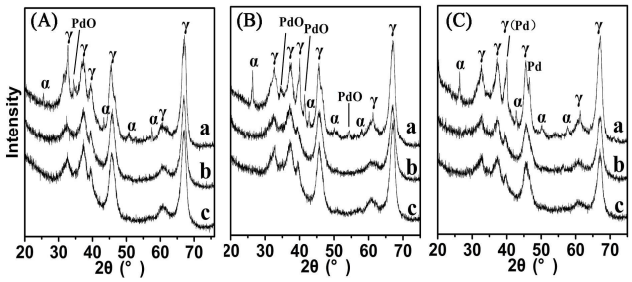

Figure 11. XRD patterns of fresh catalysts (A) used catalysts (B) and reduced catalysts (C) calcined at 1000 °C (a: Pd/CA, b: Pd/0.10AA-30 and c: Pd/0.10AA-20)

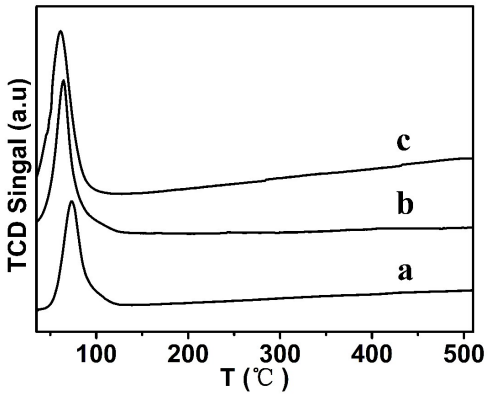

Figure 12. H_2-TPR profiles of fresh catalysts calcined at 1000 °C (a: Pd/CA, b: Pd/0.10AA-30 and c: Pd/0.10AA-20)

high thermal stability of catalysts and high dispersion and small size of active component.

H_2-TPR profiles were employed to investigate the reducibility of catalysts [44]. Figure 12 shows the H_2-TPR results of catalysts calcined at 1000 °C. H_2-TPR spectra of Pd/CA exhibits a reduction peak at 73 °C, which can be assigned to the reduction of the PdO. Pd/0.10AA-30 and Pd/0.10AA-20 exhibit a reduction peak of PdO at 64 and 60 °C, respectively, which is much lower than that of Pd/CA.

The result can be attributed to the larger surface area that make PdO disperse more easier so as to reduce its reduction temperature.

4. Conclusions

In an acetic acid assisted sol-gel system, by adjusting the mole ratio of n(acetic acid)/n(Al) and the synthesis temperature to control the competition of the colloidal surface free energy (*F*) and the free energy self-assemble (ΔG), mesoporous alumina with different morphologies and textures have been synthesized. When the mole ratio of n(acetic acid)/n(Al) set as 0.10, with the formation and aging temperature of precursor solution at 30 °C, high thermal stability NSMA was obtained with the diameter between 100-300 nm and dispersed well even the calcination temperature up to 1100 °C; highly ordered mesoporous γ-Al_2O_3 with high specific surface area, crystalline and highly thermal stability was synthesized while the synthesis temperature was 20 °C, and a certain ordered structure could still be distinctly seen at 1000 °C. Furthermore, taking as-synthesized NSMA and OMA as carriers, the Pd-supported catalysts with high thermal stability were obtained, and the active component of which was small-sized and high dispersion, so the catalytic activity of both for CO and C_3H_6 oxidation were obviously higher than commercial alumina.

Acknowledgements

The authors are grateful to financial support from the Natural Science Foundation of Fujian province (No.2104J01032) and National High-tech R&D Program of China (863 Program) (2015AA03A402).

References

1. G. J. A. A. Soler-Illia, C. Sanchez and B. Lebeau, *J. Patarin, Chem. Rev.*, 2002, **102**, 4093-4138.
2. A. Ivanova, D. Fattakhova-Rohlfing, B. E. Kayaalp, J. Rathouský and T. Bein, *J. Am. Chem. Soc.*, 2014, **136**, 5930-5937.
3. Y. Wang, W. Li, Y. Xia, X. Jiao and D. Chen, *J. Mater. Chem.,* 2014, **2**, 15124-15131
4. W. Cai, Y. Hu, J. Yu, W. Wang, J. Zhou and M. Jaroniec, *RSC Adv.*, 2015, **5**, 7066-7073.
5. P. Tang, Y. Chai, J. Feng, Y. Feng, Y. Li and D. Li, J. *Appl. Catal. A-Gen*., 2014, **469**, 312-319.
6. N. Kawasaki, F. Ogata and H. Tominaga, *J. Hazard. Mater.,* 2010, **181**, 574-579.
7. S. Singh, V. C. Srivastava , T. K. Mandal and I. D. Mall, *RSC. Adv.*, 2014, **4**, 50801-50810.
8. L. Zhang, X. Jiao, D. Chen and M. Jiao, *Eur. J. Inorg. Chem.*, 2011, **2011**, 5258-5264.
9. X. Fang, C. Ye, X. Peng, Y. Wang, Y. Wu and L. Zhang, *J. Mater. Chem.,* 2003, **13**, 3040-3043.
10. Y. Mathieu, B. Lebeau and V. Valtchev, *Langmuir*, 2007, **23**, 9435-9442.
11. J. Corrochano, C. Cerecedo, V. Valcárcel, M. Lieblich and F. Guitián, *Mater. Lett*., 2008, **62**, 103-105.
12. Y. Li, W. Shen, *Chem. Soc. Rev.*, 2014, 43, 1543.
13. J. Gascon, J. R. van. Ommen, J. A. Moulijn and F. Apteijn. *Catal. Sci. Technol.,* 2015, **5**, 807-817.
14. K. Niesz, P. Yang and G.A. Somorjai, *Chem. Commun*., 2005, **15**, 1986-1987.
15. Q. Yuan, A. Yin, C. Luo, L. Sun, Y. Zhang, W. Duan, H. Liu and C. Yan, *J. Am. Chem. Soc.*, 2008, **130**, 3465-3472.
16. F. Huang, Y. Zheng, G.H. Cai, Y. Zheng, Y.H. Xiao and K.M. Wei, *Scripta Mater,* 2010, **63**, 339-342.
17. F. Huang, Y. Zheng, Y. Xiao, Y. Zheng, G. Cai and K. Wei, *Mater. Lett.,* 2011, **65**, 244-246.
18. Q. Sun, Y. Zheng, Z. Li, Y. Zheng, Y. Xiao and G. Cai, *Mater. Lett.,* 2012, **84**, 44-47.
19. X. Zhao, Y. Zheng, Y. Zheng, Y. Zhan and X. Zheng, *RSC. Adv.,* 2014, **4**, 12497-12505.
20. F. Huang, Y. Zheng, Z. Li, Y. Xiao, Y. Zheng, G. Cai and K. Wei, *Chem. Comm.,* 2011, **47**, 5247-5249.
21. H. Keskinen, J. M. Mäkelä and R. Heikkinen, *Catal. Lett.,* 2007, **119**, 172-178.
22. Q. Yuan, H. Duan, L. Li, Z. Li, W. Duan, L. Zhang, W. Song and C. Yan, *Adv. Mater.*, 2010, **22**, 1475-1478.
23. H. C. Lee, H. J. Kim, C. H. Rhee, K. H. Lee, J. S. Lee and S. H. Chung, *Micropor. Mesopor. Mater.*, 2005, **79**, 61-68.
24. R. Zhao, F. Guo, Y. Hu and Zhao, H, *Micropor. Mesopor. Mater.*, 2006, **93**, 212-216.
25. P. Bai, P. Wu, Z. Yan, X. S. Zhao, *Sci. Adv. Mater.*, 2011, **3**, 994-1003.
26. K. C. W. Wu, X. Jiang and Y. Yamauchi, *J. Mater. Chem.*, 2011, **21**, 8934-8939.
27. K. Ariga, Y. Yamauchi, G. Rydzek, Q. Ji, Y. Yonamine, K. C. W. Wu, J. P. Hill, *Chem. Lett.*, 2014, **43**, 36-68.
28. Y. T. Liao, C. W. Huang, C. H. Liao, J. C. S. Wu and K. C. W. Wu, *Applied. Energy.*, 2012, **100**, 75-80.
29. H. Y. Lian, Y. H. Liang, Y. Yamauchi and K. C. W. Wu, *J. Phys. Chem. C.*, 2011, **115**, 6581-6590.
30. C. Yu, J. Fan, B. Tian and D. Zhao. *Chem. Mater.*, 2004, **16**, 889-898.
31. C. Liu, L. Li, H. Song and X. Chen, *Chem. Commun.,* 2007, **7**, 757-759.
32. K. L. Martena, S. M. Grant and M. Jaroniec, *ACS. Appl. Mater. Inter.,* 2012, **4**, 3738-3744.
33. L. Xu, H. Song and L. Chou, *Int. J. Hydrogen Energ.*, 2013, **38**, 7307-7325.

34. F. Huang, Y. Zheng, Y. Xiao, Y. Zheng, G. Cai and K. Wei, *Mater. Lett.,* 2011, **65**, 244-246.
35. Z. Zhang and T. J. Pinnavaia, *J. Am. Chem. Soc.*, 2002, **124**, 12294-12301.
36. J. Fan, S. W. Boettcher and G. D. Stucky, *Chem. Mater.*, 2006, **18**, 6391-6396.
37. R. Beye, M. Verwerft and J. T. M. De Hosson, *Acta. Mater.*, 1996, **44**, 4225-4231.
38. Y. Wang, P.M. Bronsveld and J.T.M. De Hosson, *J. Eur. Ceram. Soc.,* 1998, **18**, 299-304.
39. A. Abidli, S. Hamoudi and K. Belkacemi, *Dalton. T.*, 2015, **44**, 9823-9838.
40. T. Xie, L. Sh, J. Zhang and D. Zhang, *Chem. Commun.*, 2014, **50**, 7250-7253.
41. K.S. Kim, A.F. Gossmann and N. Winograd, *Anal. Chem.*, 1974, **46** 197.
42. S. Sareen, V. Mutreja, S, Singh and B. Pal, *RSC Adv.*, 2015, **5**, 184-190.
43. S. Lin, L. Yang, X. Yang and R. Zhou. *Chem. Eng. J.*, 2014, **247**, 42-49.
44. T. Xie, X. Zhao, J. Zhang, L. Shi and D. Zhang, *Int. J. Hydrogen Energ.*, 2015, **40**, 9685-9695.